

Chemical trends in the high thermoelectric performance of the pyrite-type dichalcogenides ZnS₂, CdS₂, and CdSe₂

Tiantian Jia^{1,2,4}, Jesús Carrete³, Georg K. H. Madsen³, Yongsheng Zhang^{1,5,*} and Su-Huai Wei^{2,†}

¹Key Laboratory of Materials Physics, Institute of Solid State Physics, Hefei Institutes of Physical Science (HFIPS), Chinese Academy of Sciences, 230031 Hefei, China

²Beijing Computational Science Research Center, 100193 Beijing, China

³Institute of Materials Chemistry, TU Wien, A-1060 Vienna, Austria

⁴University of Science and Technology of China, 230026 Hefei, China

⁵Advanced Research Institute of Multidisciplinary Sciences, Qufu Normal University, 273165 Qufu, China



(Received 8 March 2022; revised 12 May 2022; accepted 13 June 2022; published 27 June 2022)

The thermoelectric (TE) properties of the three pyrite-type IIB-VIA₂ dichalcogenides (ZnS₂, CdS₂, and CdSe₂) are systematically investigated and compared with those of the prototype ZnSe₂ to optimize their TE properties. Using the phonon Boltzmann transport equation, we find that they all have ultralow lattice thermal conductivities. By analyzing their vibrational properties, this is attributed to soft phonon modes derived from the loosely bound rattlinglike metal atoms and to strong anharmonicity caused by the vibrations of all atoms perpendicular to the strongly bound nonmetallic dimers. Additionally, by correlating those properties along the series, we elucidate several chemical trends. We find that the heavier atom masses, larger atomic displacement parameters, and longer bond lengths between metal and nonmetal atoms can be beneficial to the looser rattling behaviors of the metal atoms and therefore lead to the softer phonon modes and that the stronger nonmetallic dimer bonds can boost the anharmonicities, both leading to the lower thermal conductivities. Furthermore, we find that all three compounds have complex energy isosurfaces at valence and conduction band edges that simultaneously allow for large density-of-states effective masses and small conductivity effective masses for both *p*- and *n*-type carriers. Consequently, the calculated TE figures of merit (*ZT*) can reach large values for both *p*- and *n*-type doping. In this paper, we illustrate the effects of the rattlinglike metal atoms and the localized nonmetallic dimers on the thermal transport properties and the importance of different carrier effective masses to electrical transport properties in these pyrite-type dichalcogenides, which can be used to predict and optimize the TE properties of other TE compounds in the future.

DOI: [10.1103/PhysRevB.105.245203](https://doi.org/10.1103/PhysRevB.105.245203)

I. INTRODUCTION

The thermoelectric (TE) conversion efficiency of a device depends on the dimensionless figure of merit $ZT = S^2\sigma T/\kappa$, where S is the Seebeck coefficient, σ is the electrical conductivity, T is the absolute temperature, and κ is the thermal conductivity including charge carrier (κ_e) and lattice (κ_l) contributions. Promising TE materials must have high thermopower factors ($PF = S^2\sigma$) and low thermal conductivities. In semiconductors, the thermal conductivity is mainly determined by phonon properties that control the lattice contribution. However, since the state-of-the-art TE materials still have relatively low ZT values or contain expensive elements, the commercial applications of TE devices are limited. Two major strategies are currently used to increase the ZT values of TE materials: (i) using band structure engineering to improve the PF (e.g., enhancing the Seebeck coefficient or raising the electrical conductivity by generating multiple-band resonant states, or shifting Fermi energy

to proper energy position through alloying or doping in PbTe [1], Mg₂Si_{1-x}Sn_x [2], Sb₂Te₃ [3], etc.) [4–8] and/or (ii) using defect or nanostructure engineering to decrease κ_l (e.g., enhancing anharmonicity or increasing phonon scatterings by decreasing the dimensionality in some systems, such as two-dimensional (2D) TiSe [9], SnS₂ nanosheets [10], carbon-nitride nanosheets [11], phosphorene [12], B-/N-graphdiyne [13,14], and the group-13 metal chalcogenides monolayers [15]) [16–19]. Additionally, owing to the development of computational methodologies, high-throughput methods have been used to seek high-performance TE materials [20–23].

Recently, the pyrite-type compounds FeX₂ ($X = S, Se, \text{ and } Te$) [24–26], PtSb₂ [27], and MnTe₂ [28] have shown promising TE performance based on either first-principles studies or experimental measurements. Moreover, through our previous high-throughput calculations [29], we predicted that a distinct pyrite-type IIB-VIA₂ dichalcogenide (ZnSe₂) has an excellent TE performance due to the complex electronic energy isosurfaces and the existence of the rattlinglike Zn atoms around the localized Se-Se dimers that improve the electronic and lattice contributions, respectively [30]. However, the TE properties of many other pyrite-type dichalcogenides with the

*yshzhang@theory.issp.ac.cn

†suhuaiwei@csrc.ac.cn

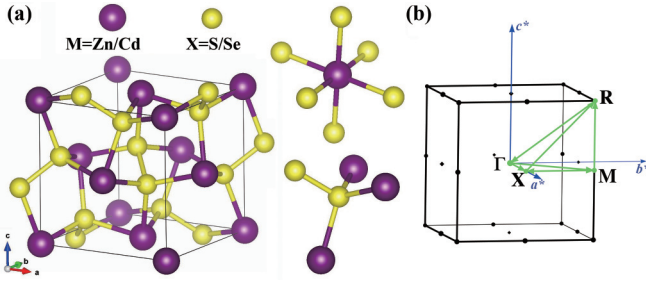


FIG. 1. (a) Crystal structures and bonds between atoms in the pyrite-type IIB-VIA₂ dichalcogenides [Pa $\bar{3}$ -MX₂, M = transition metal (Zn and Cd), X = S and Se]. The Wyckoff positions are $4a$ (0,0,0) for M and $8c$ (u,u,u) for X , where u is the Wyckoff pyrite parameter. In this structure, each M atom has six X neighbors, whereas each X atom binds with three M and one X atoms, and the neighboring X atoms form the X - X dimers. (b) The corresponding first Brillouin zone and its high-symmetry points.

same prototype remain to be investigated. Therefore, we set out to explore the TE performances of three other pyrite-type IIB-VIA₂ dichalcogenides: ZnS₂, CdS₂, and CdSe₂, which were successfully synthesized at high pressures (6.5–8.9 GPa) [31], and to compare their properties with ZnSe₂ to identify the chemical trends.

The crystal structure of the pyrite-type dichalcogenides (MX₂, M = transition metal, X = S and Se) is in the prototype rock-salt, where the metal atom and the center of nonmetallic dimer occupy the Na and Cl sites, respectively, and belongs to the Pa $\bar{3}$ space group, as shown in Fig. 1(a). Thus, not only the structure but also the transport coefficients of these compounds are isotropic. In this paper, we investigate the thermal and electrical transport properties of three pyrite-type IIB-VIA₂ dichalcogenides (ZnS₂, CdS₂, and CdSe₂) and evaluate their TE performances. By calculating and analyzing their phonon properties, we find that like the previously studied ZnSe₂ [30], all three pyrite-type dichalcogenides have easily identifiable localized high-frequency optical phonons contributed by their strongly covalently bound nonmetallic dimers and soft phonon modes contributed by their rattling metal atoms. Furthermore, they all have strong anharmonicities and low thermal conductivities ($< 2 \text{ W m}^{-1} \text{ K}^{-1}$ at 300 K). Additionally, we find some chemical trends in that (i) heavier atom masses, larger atomic displacement parameters (ADPs), and longer bond lengths between metal and nonmetal atoms can result in the softer phonon frequencies; (ii) the vibrations of all atoms perpendicular to the nonmetallic dimers can contribute to their strong anharmonicities, and the stronger the nonmetallic dimer bonding, the more obvious the anharmonicity. Furthermore, we find that all three compounds show promising electrical transport properties for both p - and n -type doping, owing to their large density-of-states (DOS) effective masses and small conductivity effective masses, which can be explained in terms of the complex nonspherical isoenergy Fermi surfaces in both the valence and conduction bands. Finally, the low lattice thermal conductivity and promising electrical transport properties contribute to their excellent TE performances. Our work can help and guide experimental and theoretical researchers to find high-performance TE materials.

II. COMPUTATIONAL METHODOLOGY

The electronic properties are calculated by means of density functional theory (DFT) as implemented in the Vienna *Ab initio* Simulation Package (VASP) [32] with the projector augmented-wave method [33]. Their electronic exchange and correlation energies are accounted for through the generalized gradient approximation of Perdew, Burke, and Ernzerhof (PBE) [34]. The energy cutoffs for the plane-wave expansion are 420 eV. To calculate the phonon vibrational properties, the crystal structures are relaxed with convergence parameters: a $8 \times 8 \times 8$ k-point mesh, the convergence of the total energies to $< 10^{-8}$ eV, and the force components of each atom $< 10^{-4}$ eV/Å. In addition, $2 \times 2 \times 2$ supercells are used for the second- and third-order interatomic force constant calculations by resolving the irreducible set of atomic displacements, as implemented in the PHONOPY software package [35] and the THIRDORDER.PY script [36]. The Born effective charges and dielectric tensors are also extracted from the DFT calculations.

The lattice thermal conductivities (κ_l) as functions of temperature (T) are calculated using the linearized phonon Boltzmann transport equation (BTE):

$$\kappa_l^{\alpha\beta} = \sum_{\mathbf{sq}} \hbar \omega_{\mathbf{sq}} \frac{\partial f_{0,ph}}{\partial T} v_{\alpha}^p(\omega_{\mathbf{sq}}) v_{\beta}^p(\omega_{\mathbf{sq}}) \tau^p(\omega_{\mathbf{sq}}), \quad (1)$$

as implemented in the ALMABTE code [37]. Here, α and β ($\alpha, \beta = x, y, z$) are the tensor indices, s is the index of phonon branches, \mathbf{q} is the wave vector, \hbar is the reduced Planck constant, ω is the phonon frequency, $f_{0,ph}$ is the Bose-Einstein distribution function, $v^p(\omega)$ is the phonon velocity, and $\tau^p(\omega)$ is the phonon relaxation time. Interatomic interactions up to the fifth coordination shell are considered, and a $7 \times 7 \times 7$ Γ -centered grid is used to solve the phonon BTE.

The electrical transport properties (σ/τ , S , and κ_e) as functions of carrier concentration and temperature are calculated using the BOLTZTRAP2 code [38]. The carrier relaxation time (τ) is evaluated including the contributions from the acoustic phonon scatterings (τ_a) and the polar optical phonon scatterings (τ_o), as $\frac{1}{\tau} = \frac{1}{\tau_a} + \frac{1}{\tau_o}$. Here, τ_a and τ_o can be calculated using the deformation potential theory proposed by Bardeen and Shockley [39] and the formula of Callen [40,41], respectively:

$$\tau_a = \frac{2^{1/2} \pi \hbar^4 \rho v_l^2}{3 E_d^2 (m_d^* k_B T)^{3/2}} \frac{F_0(\eta)}{F_{1/2}(\eta)},$$

$$F_x(\eta) = \int_0^{\infty} \frac{E^x}{1 + \exp(E - \eta)} dE, \quad \eta = \frac{\mu}{k_B T}, \quad (2)$$

$$\tau_o = \frac{8\pi \hbar^2}{e^2 (2m_d^* k_B T)^{1/2} (\epsilon_{\infty}^{-1} - \epsilon_s^{-1})} \eta^{1/2}, \quad (3)$$

where k_B is the Boltzmann constant, ρ is the mass density, v_l is the longitudinal acoustic velocity, μ is the chemical potential, η is the reduced chemical potential, m_d^* is the DOS effective mass, E_d is the acoustic deformation potential, and ϵ_s and ϵ_{∞} are the static and high-frequency permittivity, respectively. Among them, v_l can be calculated from the phonon properties as $v_l = \frac{\partial \omega}{\partial k}$, m_d^* can be obtained from the electronic band structures, and E_d can be evaluated by calculating the

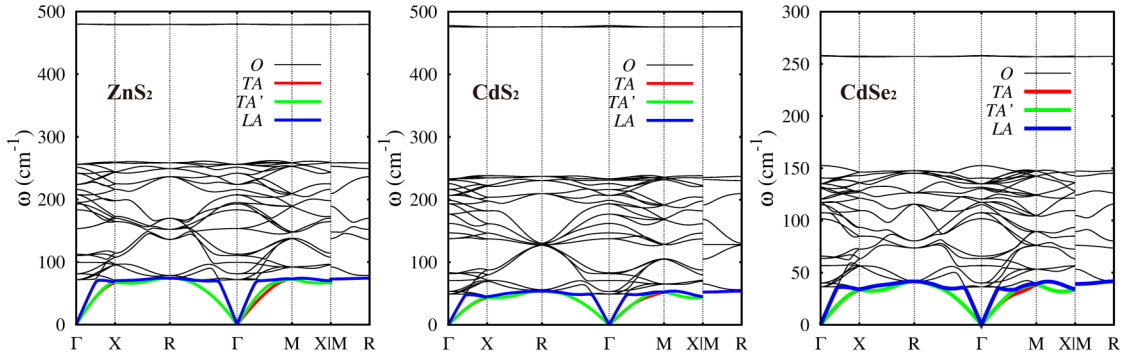


FIG. 2. Calculated phonon dispersions of ZnS₂, CdS₂, and CdSe₂ (from left to right), respectively. The red, green, and blue lines highlight two transverse (TA, TA') and one longitudinal (LA) acoustic phonon modes, respectively. The black lines represent optical (O) phonon modes.

energy change of the band extrema under volume dilation as $E_d = \Delta E / (\frac{\Delta V}{V_0})$ (where V_0 is the equilibrium lattice volume). However, since the reference of an energy level in an infinite periodic crystal is ill defined, the absolute deformation potential (E_d) of a bulk semiconductor is difficult to be evaluated. To overcome this problem, we used an approach proposed by Wei and Zunger [42], which uses the energy level of the deep core state as a reference to obtain the absolute band energy changes. This approach has been successfully implemented to theoretically evaluate the carrier relaxation times of many semiconductors (such as SnSe, SnS, CuSbS₂, and CuBiS₂) [43–46].

III. RESULTS AND DISCUSSION

A. Lattice parameters and phonon properties

For the three pyrite-type IIB-VIA₂ dichalcogenides: ZnS₂, CdS₂, and CdSe₂, the calculated lattice constants (a) are 5.997, 6.399, and 6.740 Å, which are in reasonable agreement with the experimental measurements (5.954, 6.303, and 6.615 Å) [31], and the calculated pyrite parameters (u) are 0.400, 0.406, and 0.397, consistent with the previous theoretical values [47]. To evaluate their structural stabilities under ambient pressure, we calculate their phonon dispersions along different high-symmetry lines [refer to the Brillouin zone in Fig. 1(b)], as shown in Fig. 2. Three acoustic phonon branches [two transverse (TA, TA') and one longitudinal (LA)] are highlighted. From Fig. 2, we can see that all phonon frequencies of the three dichalcogenides are real (depicted as positive), which indicates that all of them are mechanically stable under ambient pressure.

In most semiconductors, the thermal conductivities are mainly contributed by phonons. By comparing the shapes and values of the calculated phonon dispersions in the three dichalcogenides (Fig. 2), we find that they all have qualitatively similar phonon dispersion curves along different high-symmetry lines and that their phonon frequencies (ω) generally follow $\omega(\text{ZnS}_2) > \omega(\text{CdS}_2) > \omega(\text{CdSe}_2)$, with maximum values for acoustic phonons of 74.1, 53.9, and 42.3 cm⁻¹, respectively. Consequently, their speeds of sound also follow the order $v(\text{ZnS}_2) > v(\text{CdS}_2) > v(\text{CdSe}_2)$. These results are consistent with the inverse proportionality between the speed of sound and the square root of the density [48], which is dominated by the atomic mass in this case: Cd

is heavier than Zn, and Se is heavier than S. Furthermore, we find that they all have isolated, localized high-frequency phonons and obvious bandgaps in the optical phonon regions. The ranges of those bandgaps are from 262 to 478 cm⁻¹ for ZnS₂, from 239 to 475 cm⁻¹ for CdS₂, and from 153 to 257 cm⁻¹ for CdSe₂, respectively, see Fig. 2.

By calculating the phonon DOSs (PDOSs) of the three dichalcogenides [Fig. 3(a)], we find that their isolated localized high-frequency optical phonons are only contributed by the nonmetal (X) atoms, and their low-frequency phonons are contributed by the metal (M) and nonmetal (X) atoms together. To analyze the reasons, we calculate their projected 2D electron localization function (ELF) [49] in the (001) plane, as shown in Fig. 3(b). The ELF is a measure of the extent of electronic spatial localization at a given position. Higher ELF value indicates more electronic localization (as covalent bonds, core shells, or lone pairs) [49]. From Fig. 3(b), we find that the calculated ELF values around two adjacent nonmetal (X) atoms are very large, which indicates that the three dichalcogenides all form strong covalently bound non-metallic (X - X) dimers. By analyzing the atomic vibrations, we find that their isolated localized high-frequency optical phonons mostly correspond to stretches of the strong non-metallic dimers, like the case of ZnSe₂ [30].

Low-frequency phonons in the three dichalcogenides [such as those with phonon frequencies (ω) < 262, 239, and 153 cm⁻¹ in ZnS₂, CdS₂, and CdSe₂, respectively, in Fig. 3(a)] can be further separated into two regions: (i) <147, 123, and 73 cm⁻¹ in ZnS₂, CdS₂, and CdSe₂, respectively, where most of the contribution comes from M ; and (ii) at higher frequencies, where the vibrations of X atoms dominate. To explore the reasons, we calculate the ADPs in the three dichalcogenides, as shown in Fig. 3(c). The ADPs measure the mean-square displacement amplitude of an atom about its equilibrium position in a crystal. The ADPs of different atoms along an arbitrary axis as functions of temperature can be calculated from the number of phonon excitations [35], as $\langle |u_j|^2 \rangle = \frac{\hbar}{2Nm_j} \sum_{s\mathbf{q}} (\omega_{s\mathbf{q}})^{-1} [1 + 2n_{s\mathbf{q}}(T)] |\hat{\mathbf{n}} \cdot \mathbf{e}_{s\mathbf{q}}^j|^2$, where u is the atomic displacement, j is the label for the j th atom, m is the atomic mass, N is the number of the unit cells, n is the phonon population at temperature T , $\hat{\mathbf{n}}$ is an arbitrary unit direction, and \mathbf{e} is the polarization vector of the atom j and the band s at the wave vector \mathbf{q} . By comparing the calculated ADPs of different atoms in Fig. 3(c), we find

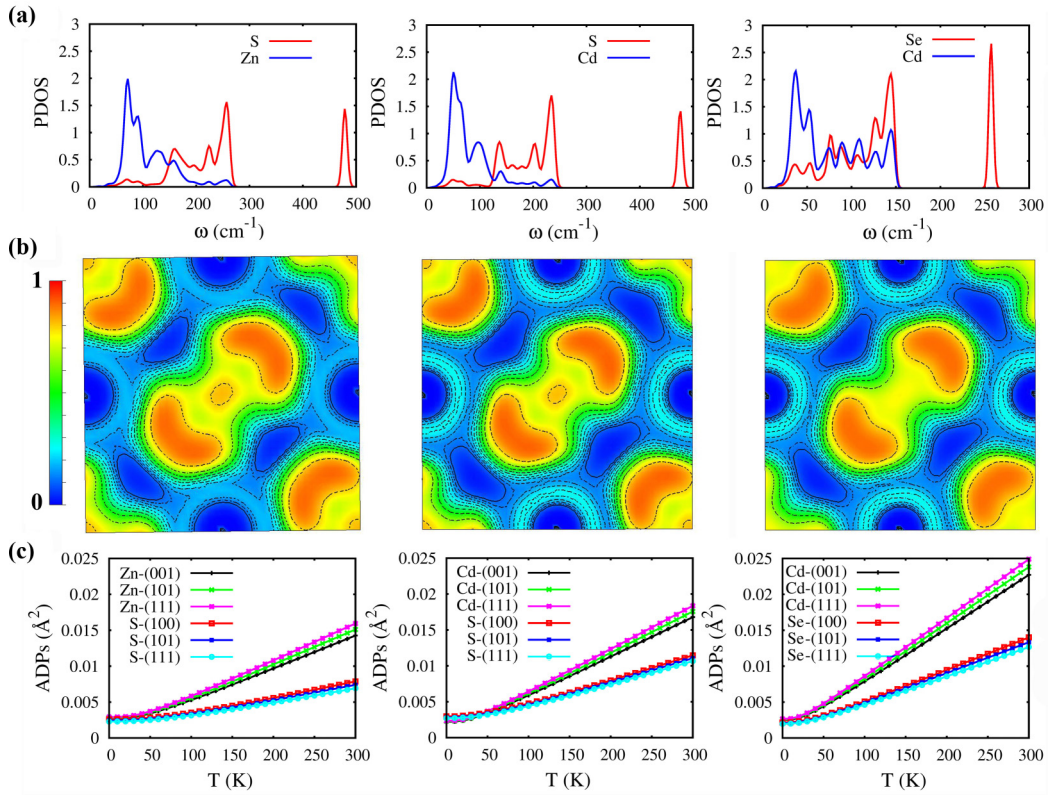


FIG. 3. (a) Calculated partial phonon densities of states (PDOSs), (b) projected two-dimensional (2D) electron localization function (ELF) in (001) plane, and (c) atomic displacement parameters (ADPs) along different directions of different atoms in ZnS₂, CdS₂, and CdSe₂ (from left to right), respectively.

that the calculated ADPs of M atoms are much larger than that of X atoms in all three dichalcogenides, and the calculated ADPs of different M atoms follow $\text{ADPs}(\text{ZnS}_2\text{-Zn}) < \text{ADPs}(\text{CdS}_2\text{-Cd}) < \text{ADPs}(\text{CdSe}_2\text{-Cd})$. This means that the M atoms are loosely bound to the X atoms and behave as the rattlinglike atoms [50] in all three dichalcogenides and that the rattling behaviors in CdSe₂ are more obvious than that in CdS₂ and ZnS₂. This can in turn explain the lower ω of M atoms than that of X atoms and the lower ω in CdSe₂ than that in CdS₂ and ZnS₂ in a way. Additionally, by calculating the bond lengths (L_{M-X}) between the rattlinglike metal atom (M) and nonmetal atom (X) (as $L_{\text{Zn-S}} = 2.544$ Å, $L_{\text{Cd-S}} = 2.733$ Å, and $L_{\text{Cd-Se}} = 2.851$ Å, which follow $L_{\text{Zn-S}} < L_{\text{Cd-S}} < L_{\text{Cd-Se}}$), and comparing with the calculated phonon properties (ω and v) in the three compounds, we can conclude that the L_{M-X} have an opposite tendency from the calculated ω and v . This means that the longer L_{M-X} can contribute to the softer phonon properties, and another main reason for the lower ω and smaller v of CdSe₂ may be the longer L_{M-X} of CdSe₂ than CdS₂ and ZnS₂.

B. Anharmonicities

In addition to the phonon frequency and sound velocity, authors of many previous studies have shown that the Grüneisen parameter ($\gamma = -\frac{V}{\omega} \frac{\partial \omega}{\partial V}$) is an important descriptor of κ_l [51,52]. Therefore, we calculate and compare the values of γ at different phonon modes in the three dichalcogenides (as shown in Fig. 4). We find their calculated γ

follows $\gamma(\text{ZnS}_2) > \gamma(\text{CdS}_2) > \gamma(\text{CdSe}_2)$, and the maximum Grüneisen parameters (γ_m) in acoustic phonons are 4.60, 3.18, and 2.72 for ZnS₂, CdS₂, and CdSe₂, respectively, which are comparable with other excellent TE materials with strong anharmonicity (such as AgSbTe₂ and SnSe, their Grüneisen parameters being 2.05 [53] and 4.1 [54], respectively). This means that, like ZnSe₂ (whose calculated γ_m is 4.6) [30], the three dichalcogenides also show strong anharmonicity.

To explore the origins of the strong anharmonicity in these dichalcogenides, we analyze and compare the calculated γ at different phonon modes in the same compound (in Fig. 4). We find that, although the calculated ω of two transverse acoustic phonon branches (TA and TA') along the ΓM line in the same compound are very close, the calculated γ of those TA and TA' branches are obviously different (the calculated γ of the TA branch is far higher than those of the TA' branch). By analyzing the vibration modes of atoms in those TA and TA' branches along the ΓM line (as shown in Fig. S1 in the Supplemental Material [55]), we find that the vibrations of all atoms in the TA branch are primarily perpendicular to the nonmetallic dimers, but the angles between the vibrations of all atoms in the TA' branch and the direction of the nonmetallic dimers are close to 54.7°. Therefore, combining that with the analysis of ZnSe₂, we can infer that the vibrations of all atoms perpendicular to the bonding direction of the strong covalently bound nonmetallic dimers can result in a large change of the pyrite parameters (u) [30] and the strong anharmonicity at the acoustic phonons, and the existence of the strong covalently bound nonmetallic dimer has an important influence on the

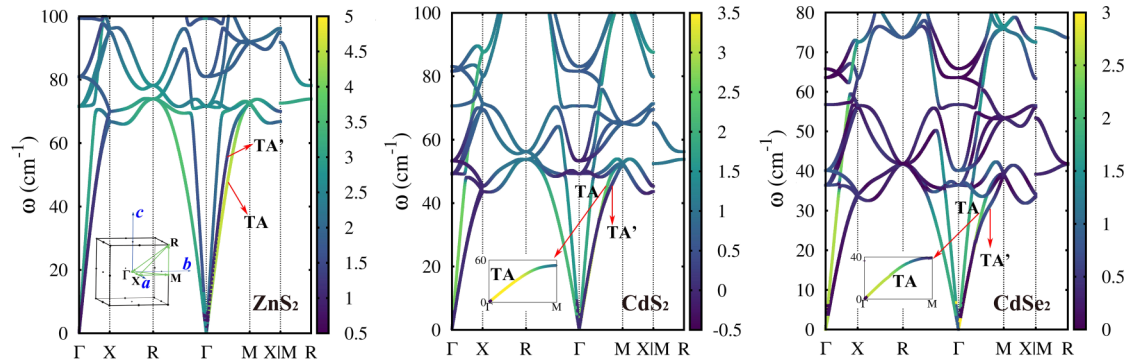


FIG. 4. Calculated anharmonicity parameters (γ) at different phonon modes (the color denotes the values of γ) for ZnS_2 , CdS_2 , and CdSe_2 (from left to right), respectively.

strong anharmonicity in these pyrite-type dichalcogenides. Furthermore, by comparing the bond lengths between two adjacent S atoms in S-S dimers ($L_{\text{S-S}}$) in ZnS_2 and CdS_2 , we find that their $L_{\text{S-S}}$ are 2.079 and 2.086 Å, respectively. The $L_{\text{S-S}}$ in ZnS_2 is shorter than CdS_2 , which means that the bond strengths of the nonmetallic dimers in ZnS_2 are stronger than CdS_2 . Comparing the calculated $L_{\text{S-S}}$ with the calculated γ , we can infer that the stronger nonmetallic dimers are beneficial to the stronger anharmonicity in these pyrite-type dichalcogenides.

C. Lattice thermal conductivities

From the analyses above, we can see that the three dichalcogenides (ZnS_2 , CdS_2 , and CdSe_2) all have soft phonon modes and strong anharmonicity, which can contribute to their low lattice thermal conductivity (κ_l). To verify it, we calculate the κ_l of ZnS_2 , CdS_2 , and CdSe_2 at different temperatures. The results, presented in Fig. 5, reveal that the calculated κ_l at 300 K are 1.55, 1.47, and 0.75 $\text{W m}^{-1} \text{K}^{-1}$ for ZnS_2 , CdS_2 , and CdSe_2 , respectively. By comparing the calculated κ_l with the calculated minimum lattice thermal conductivity (κ_{min}) based on the Ioffe-Regel criterion [56] (the calculated κ_{min} at 300 K are 0.13, 0.10, and 0.07 $\text{W m}^{-1} \text{K}^{-1}$ for ZnS_2 , CdS_2 , and CdSe_2 , respectively), we find that the calculated κ_l are much higher than the calculated κ_{min} , which supports our choice of the phonon BTE method. Additionally,

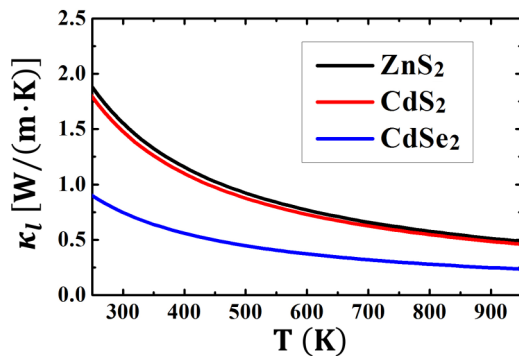


FIG. 5. Calculated lattice thermal conductivities (κ_l) at different temperatures for ZnS_2 (black line), CdS_2 (red line), and CdSe_2 (blue line), respectively.

the calculated κ_l are lower than the thermal conductivity of PbTe with good TE performance ($2.4 \text{ W m}^{-1} \text{K}^{-1}$) [57], which means that all three dichalcogenides have low lattice thermal conductivities and are consistent with our analyses of their phonon properties. Furthermore, since the heavy atom masses, large ADPs, and long bond lengths between metal and nonmetal atoms can contribute to the soft phonon properties, the speeds of sound in the three dichalcogenides follow $v(\text{ZnS}_2) > v(\text{CdS}_2) > v(\text{CdSe}_2)$. Since the strong nonmetallic dimers can be beneficial to the strong anharmonicities, their anharmonicities follow $\gamma_m(\text{ZnS}_2) > \gamma_m(\text{CdS}_2) > \gamma_m(\text{CdSe}_2)$. As a result, according to the approximate relationship between κ_l and (v, γ) as $\kappa_l \propto \frac{v^3}{\gamma^2}$ [58], their calculated lattice thermal conductivities have the trend $\kappa_l(\text{ZnS}_2) \sim \kappa_l(\text{CdS}_2) > \kappa_l(\text{CdSe}_2)$.

D. Electronic band structures

To explore the TE performance of the three dichalcogenides (MX_2), we also calculate their electronic band structures and evaluate their electrical transport properties. Figure 6(a) shows the PBE-calculated electronic band structures of ZnS_2 , CdS_2 , and CdSe_2 from left to right, respectively. From Fig. 6(a), we find that the three isoelectronic compounds have very similar band structure shapes near their Fermi levels. Their valence band maxima (VBM) are also all located at the Γ point with twofold band degeneracy [as shown in Fig. 6(a) as B1, B2] and their conduction band minima (CBM) are all located at the P point along the R - Γ line [as shown in Fig. 6(a)] with a resulting large degeneracy (8) due to symmetry. Their calculated indirect bandgaps are 1.41, 1.15, and 0.59 eV, respectively. By calculating their partial charge densities at the VBM and CBM (as shown in Fig. S2 in the Supplemental Material [55]), we find that their electronic states at the VBM are mainly contributed by the p electrons in nonmetal atoms (X_p) and the electronic states at the CBM are mainly contributed by the antibonding states of s electrons in metal atoms (M_s) and s electrons in nonmetal atoms (X_s). Since the calculated atomic energy levels [59,60] of the outermost valence p electrons are $E(\text{S}_{3p}) = -7.112 \text{ eV}$ and $E(\text{Se}_{4p}) = -6.660 \text{ eV}$, i.e., $E(\text{S}_{3p}) < E(\text{Se}_{4p})$, the energy levels at the VBM in MS_2 will be lower than those in MSe_2 , which can result in a bigger bandgap of MS_2 than MSe_2 . Moreover, since the Zn-S bond lengths in

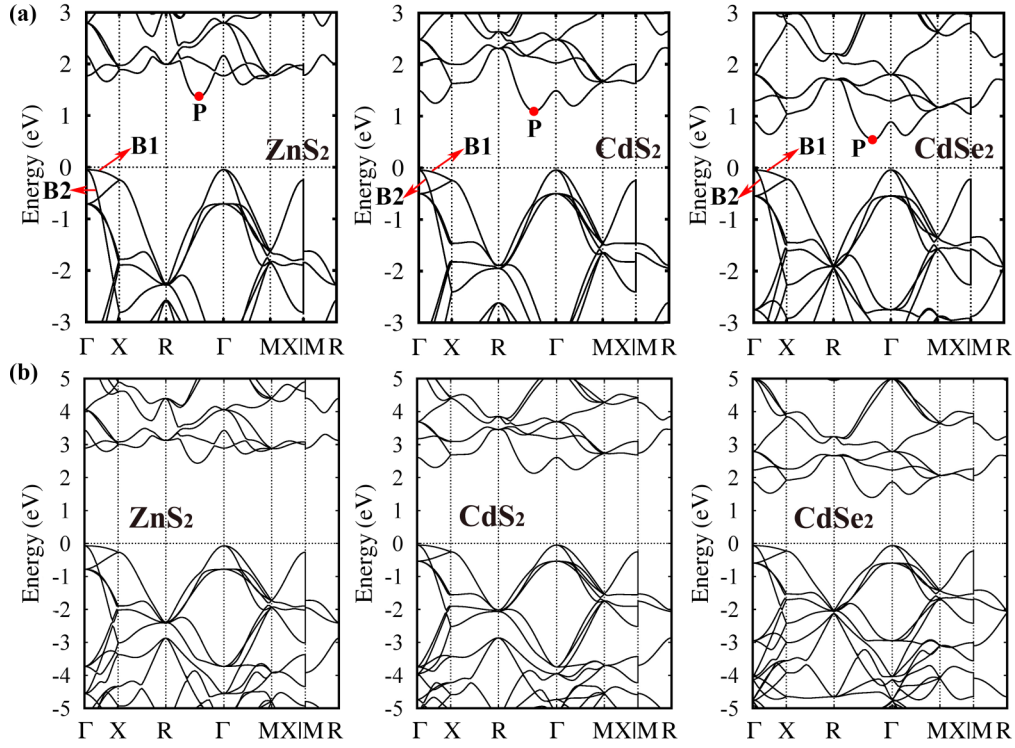


FIG. 6. (a) The PBE-calculated and (b) the HSE06-calculated electronic band structures of ZnS₂, CdS₂, and CdSe₂ (from left to right), respectively.

ZnS₂ ($L_{\text{Zn-S}} = 2.544 \text{ \AA}$) are shorter than the Cd-S bond lengths in CdS₂ ($L_{\text{Cd-S}} = 2.733 \text{ \AA}$), the antibonding strength of Zn_{4s}-S_{3s} in ZnS₂ is stronger than Cd_{5s}-S_{3s} in CdS₂, which can cause the energy levels at the CBM in ZnS₂ to be higher than in CdS₂ and the bandgap in ZnS₂ to be bigger than in CdS₂.

In addition, we compare the band structure shapes of the heavy (B1) and light (B2) bands along the Γ -X direction in the same compound, and we find that the calculated carrier effective masses ($m_{\alpha\beta}^* = \hbar^2 \left[\frac{\partial^2 E(k)}{\partial k_\alpha \partial k_\beta} \right]^{-1}$) along the Γ -X direction are $7.38m_0$, $4.51m_0$, and $5.47m_0$ for B1 bands, and $0.24m_0$, $0.27m_0$, and $0.22m_0$ for B2 bands in ZnS₂, CdS₂, and CdSe₂, respectively (as listed in Table I, where m_0 is the electron rest mass), which means that the three dichalcogenides can provide both light and heavy p -type carriers simultaneously. However, by comparing the calculated $m_{\alpha\beta}^*$ at the CBM in the same compound along different directions (in Table II), we find that all calculated $m_{\alpha\beta}^*$ at the CBM are similar and smaller than m_0 , which means that the three dichalcogenides can provide light n -type carriers and large symmetry degeneracy (8) simultaneously.

E. Electrical transport properties

Since the PBE is well known for underestimating the bandgaps of semiconductors and insulators, we further calculate the electronic band structures and bandgaps of the three dichalcogenides using the Heyd-Scuseria-Ernzerhof (HSE06) [61,62] method [as shown in Fig. 6(b)]. Comparing Figs. 6(b) and 6(a), we find that all the HSE06-calculated band features near the Fermi level are like the PBE-calculated results, and

the HSE06-calculated bandgaps are bigger than the PBE-calculated results and are 2.53, 2.18, and 1.47 eV for ZnS₂, CdS₂, and CdSe₂, respectively, which are in good agreement with the bandgaps calculated by the previous GW study [47]. Therefore, in this paper, to evaluate the electrical transport properties of the three dichalcogenides more accurately, we manually change their bandgaps to their HSE06-calculated values but keep the PBE-calculated band structure shapes. Afterwards, by solving the electron BTE, the electrical transport properties of the three dichalcogenides at different carrier concentrations and temperatures are evaluated with the BOLTZTRAP2 code [38]. The calculated Seebeck coefficients

TABLE I. The carrier effective masses ($m_{\alpha\beta}^*$) of different energy valleys along different directions (\vec{D}) in ZnS₂, CdS₂, and CdSe₂, respectively.

P	\vec{D}	$m_{\alpha\beta}^* (m_0)$								
		ZnS ₂			CdS ₂			CdSe ₂		
		VBM	VBM	CBM	VBM	VBM	CBM	VBM	VBM	CBM
Γ	$\vec{\Gamma X}$	7.38	0.24		4.51	0.27		5.47	0.22	
	$\vec{\Gamma M}$	0.86	0.31		0.91	0.36		0.79	0.29	
	$\vec{\Gamma R}$	0.46	0.46		0.51	0.51		0.43	0.43	
P	$\vec{P_x}$			0.50			0.53			0.41
	$\vec{P_{xy}}$			0.51			0.54			0.43
	$\vec{P\Gamma}$			0.51			0.55			0.45

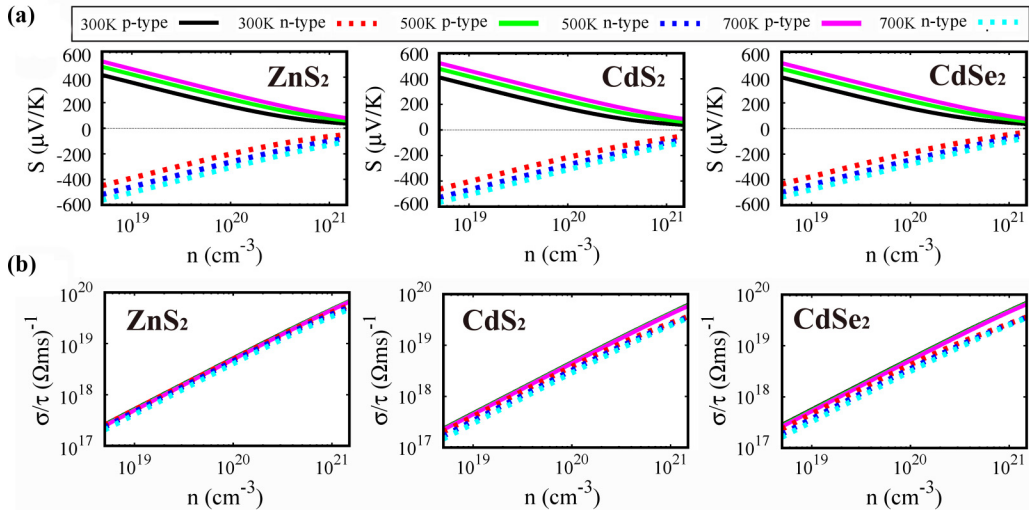


FIG. 7. (a) Calculated Seebeck coefficients S and (b) electrical conductivities with respect to relaxation time σ/τ in ZnS_2 , CdS_2 , and CdSe_2 (from left to right) as functions of the carrier concentration for p - and n -type doping at 300, 500, and 700 K, respectively.

(S) and electrical conductivities with respect to relaxation time (σ/τ) in ZnS_2 , CdS_2 , and CdSe_2 as functions of carrier concentration at different temperatures (300, 500, and 700 K) are shown in Figs. 7(a) and 7(b), respectively.

From Fig. 7(a), we find that the calculated absolute values of S ($|S|$) at 300 K with 10^{19} cm^{-3} carrier concentration are 359, 353, and 342 $\mu\text{V/K}$ for p -type carriers and 390, 405, and 377 $\mu\text{V/K}$ for n -type carriers in ZnS_2 , CdS_2 , and CdSe_2 , respectively, which are larger than that of the well-studied PbTe ($\sim 100 \mu\text{V/K}$ for n -type carriers) [63]. This means that all three dichalcogenides have large Seebeck coefficients. Furthermore, we find that their calculated $|S|$ are all decreased with the increase of the carrier concentration (n), which can be explained by the Mott formula, as [41]

$$S = \frac{2k_B^2}{3e\hbar^2} m_d^* \left(\frac{\pi}{3n} \right)^{2/3} T, \quad (4)$$

where m_d^* is the DOS effective mass, as $m_d^* = \sum_{N_V} \sqrt[3]{\prod_{\alpha\beta} m_{\alpha\beta}^*}$. From Eq. (4), we can see that the values of m_d^* have a significant effect on S . As reported in previous research [64], in a semiconductor with the degeneracy and nonspherical Fermi surface, m_d^* is proportional to the Fermi surface complexity factor ($N_V K^*$), as $m_d^* \propto (N_V K^*)^{2/3}$, where N_V is the energy valley degeneracy, and K^* is the anisotropy parameter. For the three dichalcogenides, since their valence band shapes of B1 at the VBM are very flat along the Γ -X direction but very steep along the Γ -M and Γ -R directions [in Fig. 6(a)], their isoenergy Fermi surfaces of B1 will be very complex, and their K^* will be very large for p -type doping. Additionally, since their symmetry degeneracies at the P point in the CBM are large (8), their N_V will be very large for n -type doping. Therefore, their large K^* and N_V can contribute to large m_d^* . Furthermore, by calculating m_d^* using the data in Table I, those of the three dichalcogenides are $1.75m_0$, $1.65m_0$, and $1.53m_0$ for p -type carriers and $4.05m_0$, $4.32m_0$, and $3.44m_0$ for n -type carriers, which have the same trend as the calculated $|S|$. This further indicates that the large

$|S|$ in the three dichalcogenides may be mainly contributed by their large m_d^* , and larger m_d^* can result in larger $|S|$.

From Fig. 7(b), we can find that the calculated σ/τ in the three dichalcogenides are all increased with the increase of carrier concentration (n), which is caused by the relationship between the electrical conductivity (σ) and n , as [41]

$$\sigma = \frac{ne^2}{m_c^*} \tau, \quad (5)$$

where m_c^* is the conductivity effective mass, as $m_c^* = \left[\frac{1}{3} \sum_{\alpha\beta} \frac{1}{m_{\alpha\beta}^*} \right]^{-1}$. From Eq. (5), the values of σ/τ are mainly decided by m_c^* and $m_{\alpha\beta}^*$. From the above analyses of electronic band structures, due to the small $m_{\alpha\beta}^*$ along different directions of B2 band at the VBM and B band at the CBM (in Table I), all three dichalcogenides have light p - and n -type carriers, which can contribute to good σ/τ for both p - and n -type doping. Furthermore, by obtaining m_c^* at different carrier concentrations and temperatures (as shown in Fig. S3 in the Supplemental Material [55]), we find that the calculated m_c^* of CdS_2 and CdSe_2 for n -type doping are increased more obviously with the increase of temperature and carrier concentration than ZnS_2 , which can be used to explain why the calculated σ/τ of ZnS_2 for n -type doping are better than that of CdS_2 and CdSe_2 at high temperatures and high carrier concentrations [as shown in Fig. 7(b)].

TABLE II. The theoretically determined longitudinal acoustic phonon velocities (v_l), absolute deformation potentials (E_d), and static and high-frequency permittivity (ϵ_s and ϵ_∞) for ZnS_2 , CdS_2 , and CdSe_2 , respectively, where ϵ_0 is the vacuum permittivity.

IIB-VIA ₂	v_l (m/s)	E_d (eV)		ϵ_s (ϵ_0)	ϵ_∞ (ϵ_0)
		p -type	n -type		
ZnS_2	5300	-1.51	-2.24	18.31	8.45
CdS_2	4297	-0.52	-2.13	15.11	7.62
CdSe_2	3441	-0.84	-2.16	19.8	11.35

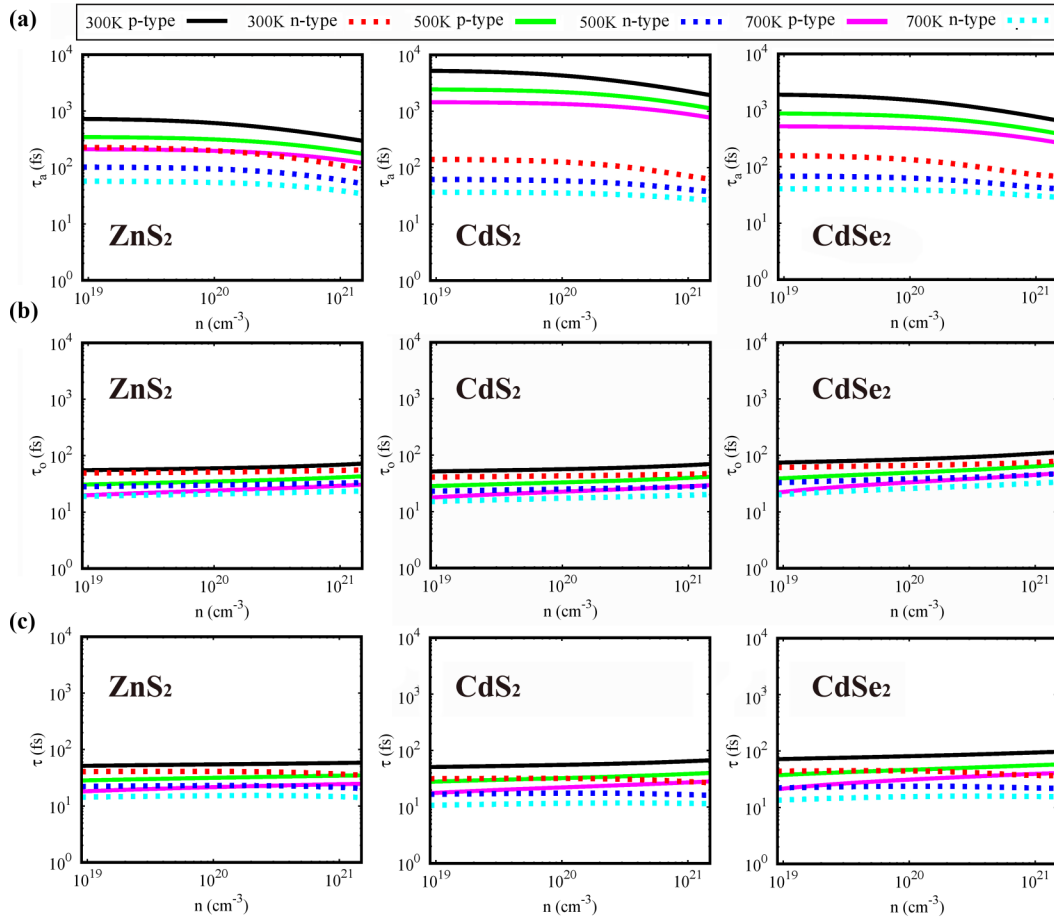


FIG. 8. (a) Calculated acoustic phonon scatterings (τ_a), (b) polar optical phonon scatterings (τ_o), and (c) total carrier relaxation times (τ) in ZnS₂, CdS₂, and CdSe₂ (from left to right) as functions of the carrier concentration for p - and n -type doping at 300, 500, and 700 K, respectively.

To complete the evaluation of the electrical transport properties of the three dichalcogenides, we need to calculate their carrier relaxation times [τ , Eqs. (2)–(3)]. The required parameters are listed in Table II [the longitudinal acoustic phonon velocities (v_l) and the absolute deformation potentials (E_d) are evaluated from the calculated phonon and electronic properties. The static and high-frequency permittivity (ϵ_s and ϵ_∞) are evaluated using the density functional perturbation theory calculations]. Then the calculated acoustic phonon scatterings (τ_a), polar optical phonon scatterings (τ_o), and total carrier relaxation times (τ) as functions of the carrier concentration at different temperatures are shown in Fig. 8.

From Fig. 8, we find that the carrier relaxation time does not rely on the carrier concentration too much. The calculated τ_a and τ_o are in the range of 10⁻¹¹ to 10⁻¹⁴ s and 10⁻¹³ to 10⁻¹⁴ s, respectively. The calculated τ_a are much longer than the calculated τ_o in all three dichalcogenides: the acoustic phonon scatterings are relatively weak, and the optical phonon scatterings dominate their electronic transport. This is due to the existence of many low-frequency optical phonons contributed by the rattling-like metal atoms in these compounds. This is like those in n -type PbTe [65]. Benefitting from the larger ϵ_∞ and smaller m_d^* in CdSe₂, the calculated τ_o are longer in CdSe₂

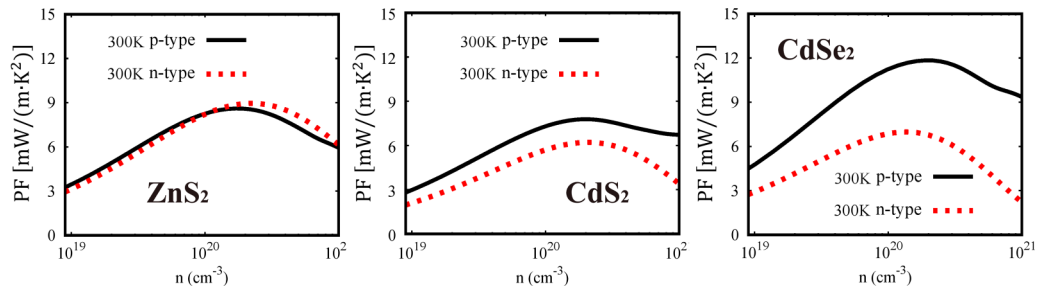


FIG. 9. Calculated power factors (PF) as functions of the carrier concentration for p - and n -type doping at 300 K in ZnS₂, CdS₂, and CdSe₂ (from left to right), respectively.

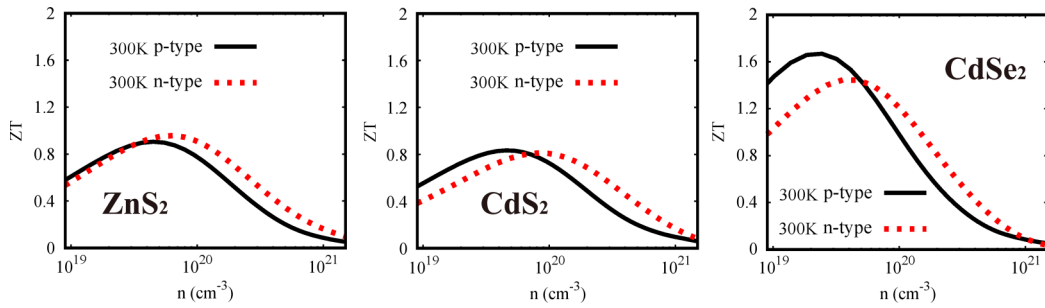


FIG. 10. Calculated figures of merit (ZT) as functions of the carrier concentration for p - and n -type doping at 300 K in ZnS_2 , CdS_2 , and CdSe_2 (from left to right), respectively.

than that in CdS_2 and ZnS_2 . Using the calculated electrical conductivities ($\sigma = \frac{q}{\tau} \times \tau$) and Seebeck coefficients (S), the power factors ($PF = S^2\sigma$) are evaluated as functions of carrier concentration at room temperature (300 K) in the three dichalcogenides, as shown in Fig. 9. We see that the calculated PF are first increased and then decreased with increasing carrier concentration (the same trend is found at high temperatures, as shown in Fig. S4 in the Supplemental Material [55]), and the maximum PF (PF_{\max}) at 300 K can reach 8.64, 7.78, and 11.84 $\text{mW m}^{-1} \text{K}^{-2}$ for p -type carriers and 9.01, 6.21, and 6.99 $\text{mW m}^{-1} \text{K}^{-2}$ for n -type carriers in ZnS_2 , CdS_2 , and CdSe_2 , respectively, which are larger than that in the well-known TE material SnSe (1.01 $\text{mW m}^{-1} \text{K}^{-2}$) [54]. This means that all three dichalcogenides have promising electrical transport properties.

F. Figures of merit

Combining the calculated thermal conductivity (κ_l and κ_e) and electrical transport properties (PF), the figures of merit (ZT) are evaluated as functions of the carrier concentration at 300 K in the three dichalcogenides (ZnS_2 , CdS_2 , and CdSe_2), as shown in Fig. 10. From it, we can see that the maximum ZT (ZT_{\max}) of the three dichalcogenides at 300 K are 0.91, 0.83, and 1.67 at 4.48×10^{19} , 4.56×10^{19} , and $2.44 \times 10^{19} \text{ cm}^{-3}$ for p -type carriers, and 0.96, 0.81, and 1.45 at 6.45×10^{19} , 8.34×10^{19} , and $3.58 \times 10^{19} \text{ cm}^{-3}$ for n -type carriers, all >0.5 . At high temperatures, the calculated ZT_{\max} in the three dichalcogenides all can be >1.5 for both p - and n -type doping, as shown in Fig. S5 in the Supplemental Material [55]. This indicates that the three dichalcogenides can be excellent TE materials over a wide temperature range for both p - and n -type doping, and they are worthy of future experimental investigations. Furthermore, due to the higher PF and the lower κ_l in CdSe_2 , the calculated ZT_{\max} for both p - and n -type doping in CdSe_2 are higher than that in ZnS_2 and CdS_2 .

IV. CONCLUSIONS

In this paper, by solving the phonon and electron BTEs, we systematically study the thermal and electrical transport properties of three pyrite-type IIB-VIA₂ dichalcogenides (ZnS_2 ,

CdS_2 , and CdSe_2). The detailed analyses of phonon properties explain that there are loosely bound rattlinglike metal atoms in all three, and the heavy atom masses, large ADPs, and long bond lengths between metal and nonmetal atoms can be beneficial to the rattling behaviors of the metal atoms and soft phonon modes. The evaluations and analyses of the Grüneisen parameters indicate that the three dichalcogenides exhibit very strong anharmonicity, traceable to the vibrations of all atoms perpendicular to the strongly bound nonmetallic dimers. The soft phonon modes and strong anharmonicities result in low lattice thermal conductivities in the three pyrite-type dichalcogenides. The calculations of electrical transport properties show that the three dichalcogenides have similar electronic band structures, and all of them can possess large DOS effective masses and small conductivity effective masses for both p - and n -type carriers. The large DOS effective masses can contribute to their high Seebeck coefficients, while the small conductivity effective masses can be beneficial to their good electrical conductivities. Their high Seebeck coefficients and good electrical conductivities guarantee their promising electrical transport properties for both p - and n -type doping. Combining their low thermal conductivities and promising electrical transport properties, their maximum ZT values at 300 K can reach 0.91, 0.83, and 1.67 for p -type doping and 0.96, 0.81, and 1.45 for n -type doping, respectively. In this paper, we show that the three pyrite-type dichalcogenides (ZnS_2 , CdS_2 , and CdSe_2) all exhibit excellent TE properties for both p - and n -type doping. Combined with previous research about ZnSe_2 , which has ZT values of 2.21 for p -type doping and 1.87 for n -type doping at high temperatures [30], we can infer that the pyrite-type IIB-VIA₂ dichalcogenides have promising TE properties. These results will be very beneficial for the design of efficient TE devices with the pyrite-type dichalcogenides.

ACKNOWLEDGMENTS

This paper is supported by National Natural Science Foundation of China, Grants No. 11774347, No. 12088101, No. 11991060, No. 12104035, and No. U1930402, and by China Postdoctoral Science Foundation, Grant No. 2021M690327, and by China Scholarship Council.

[1] J. P. Heremans, V. Jovovic, E. S. Toberer, A. Saramat, K. Kurosaki, A. Charoenphakdee, S. Yamanaka, and G. J. Snyder, *Science* **321**, 554 (2008).

[2] W. Liu, X. Tan, K. Yin, H. Liu, X. Tang, J. Shi, Q. Zhang, and C. Uher, *Phys. Rev. Lett.* **108**, 166601 (2012).

- [3] Y. C. Dou, X. Y. Qin, D. Li, L. L. Li, T. H. Zou, and Q. Q. Wang, *J. Appl. Phys.* **114**, 044906 (2013).
- [4] Y. Pei, X. Shi, A. LaLonde, H. Wang, L. Chen, and G. J. Snyder, *Nature (London)* **473**, 66 (2011).
- [5] W. J. Xie, Y. G. Yan, S. Zhu, M. Zhou, S. Populoh, K. Gałazka, S. J. Poon, A. Weidenkaff, J. He, X. F. Tang, and T. M. Tritt, *Acta Mater.* **61**, 2087 (2013).
- [6] J. Zhang, R. Liu, N. Cheng, Y. Zhang, J. Yang, C. Uher, X. Shi, L. Chen, and W. Zhang, *Adv. Mater.* **26**, 3848 (2014).
- [7] S. Chen and Z. Ren, *Mater. Today* **16**, 387 (2013).
- [8] Y. Pei, H. Wang, and G. J. Snyder, *Adv. Mater.* **24**, 6125 (2012).
- [9] A. Majumdar, S. Chowdhury, and R. Ahuja, *ACS Appl. Energy Mater.* **3**, 9315 (2020).
- [10] J. Li, J. Shen, Z. Ma, and K. Wu, *Sci. Rep.* **7**, 8914 (2017).
- [11] B. Mortazavi, F. Shojaei, M. Shahrokhi, M. Azizi, T. Rabczuk, A. V. Shapeev, and X. Zhuang, *Carbon N. Y.* **167**, 40 (2020).
- [12] G. Qin, X. Zhang, S.-Y. Yue, Z. Qin, H. Wang, Y. Han, and M. Hu, *Phys. Rev. B* **94**, 165445 (2016).
- [13] B. Mortazavi, M. Shahrokhi, X. Zhuang, and T. Rabczuk, *J. Mater. Chem. A* **6**, 11022 (2018).
- [14] B. Mortazavi, M. Makaremi, M. Shahrokhi, Z. Fan, and T. Rabczuk, *Carbon N. Y.* **137**, 57 (2018).
- [15] A. Majumdar, S. Chowdhury, and R. Ahuja, *Nano Energy* **88**, 106248 (2021).
- [16] Y. Tian, M. R. Sakr, J. M. Kinder, D. Liang, M. J. MacDonald, R. L. J. Qiu, H.-J. Gao, and X. P. A. Gao, *Nano Lett.* **12**, 6492 (2012).
- [17] Z. Li, C. Xiao, H. Zhu, and Y. Xie, *J. Am. Chem. Soc.* **138**, 14810 (2016).
- [18] Y. Lan, A. J. Minnich, G. Chen, and Z. Ren, *Adv. Funct. Mater.* **20**, 357 (2010).
- [19] K. Biswas, J. He, I. D. Blum, C. I. Wu, T. P. Hogan, D. N. Seidman, V. P. Dravid, and M. G. Kanatzidis, *Nature (London)* **489**, 414 (2012).
- [20] G. K. H. Madsen, *J. Am. Chem. Soc.* **128**, 12140 (2006).
- [21] P. Gorai, P. Parilla, E. S. Toberer, and V. Stevanović, *Chem. Mater.* **27**, 6213 (2015).
- [22] J. Yang, H. Li, T. Wu, W. Zhang, L. Chen, and J. Yang, *Adv. Funct. Mater.* **18**, 2880 (2008).
- [23] M. A. Blanco, E. Francisco, and V. Luaña, *Comput. Phys. Commun.* **158**, 57 (2004).
- [24] V. K. Gudelli, V. Kanchana, S. Appalakondaiah, G. Vaitheeswaran, and M. C. Valsakumar, *J. Phys. Chem. C* **117**, 21120 (2013).
- [25] C. Wang, Y. Niu, J. Jiang, Y. Chen, H. Tian, R. Zhang, T. Zhou, J. Xia, Y. Pan, and S. Wang, *Nano Energy* **45**, 432 (2018).
- [26] V. K. Gudelli, V. Kanchana, G. Vaitheeswaran, M. C. Valsakumar, and S. D. Mahanti, *RSC Adv.* **4**, 9424 (2014).
- [27] Y. Nishikubo, S. Nakano, K. Kudo, and M. Nohara, *Appl. Phys. Lett.* **100**, 252104 (2012).
- [28] Y. Xu, W. Li, C. Wang, Z. Chen, Y. Wu, X. Zhang, J. Li, S. Lin, Y. Chen, and Y. Pei, *J. Mater.* **4**, 215 (2018).
- [29] T. Jia, Z. Feng, S. Guo, X. Zhang, and Y. Zhang, *ACS Appl. Mater. Interfaces* **12**, 11852 (2020).
- [30] T. Jia, J. Carrete, Z. Feng, S. Guo, Y. Zhang, and G. K. H. Madsen, *Phys. Rev. B* **102**, 125204 (2020).
- [31] T. A. Bither, R. J. Bouchard, W. H. Cloud, P. C. Donohue, and W. J. Siemons, *Inorg. Chem.* **7**, 2208 (1968).
- [32] G. Kresse and J. Furthmüller, *Phys. Rev. B* **54**, 11169 (1996).
- [33] G. Kresse and D. Joubert, *Phys. Rev. B* **59**, 1758 (1999).
- [34] J. P. Perdew, K. Burke, and M. Ernzerhof, *Phys. Rev. Lett.* **77**, 3865 (1996).
- [35] A. Togo, F. Oba, and I. Tanaka, *Phys. Rev. B* **78**, 134106 (2008).
- [36] W. Li, J. Carrete, N. A. Katcho, and N. Mingo, *Comput. Phys. Commun.* **185**, 1747 (2014).
- [37] J. Carrete, B. Vermeersch, A. Katre, A. van Roekeghem, T. Wang, G. K. H. Madsen, and N. Mingo, *Comput. Phys. Commun.* **220**, 351 (2017).
- [38] G. K. H. Madsen, J. Carrete, and M. J. Verstraete, *Comput. Phys. Commun.* **231**, 140 (2018).
- [39] J. Bardeen and W. Shockley, *Phys. Rev.* **80**, 72 (1950).
- [40] H. B. Callen, *Phys. Rev.* **76**, 1394 (1949).
- [41] H. Lee, *Thermoelectrics Design and Materials* (John Wiley & Sons, Chichester, 2016).
- [42] S.-H. Wei and A. Zunger, *Phys. Rev. B* **60**, 5404 (1999).
- [43] Z. Feng, T. Jia, J. Zhang, Y. Wang, and Y. Zhang, *Phys. Rev. B* **96**, 235205 (2017).
- [44] R. Guo, X. Wang, Y. Kuang, and B. Huang, *Phys. Rev. B* **92**, 115202 (2015).
- [45] L. Xi, S. Pan, X. Li, Y. Xu, J. Ni, X. Sun, J. Yang, J. Luo, J. Xi, W. Zhu, X. Li, D. Jiang, R. Dronskowski, X. Shi, G. J. Snyder, and W. Zhang, *J. Am. Chem. Soc.* **140**, 10785 (2018).
- [46] S. Guo, T. Jia, and Y. Zhang, *J. Phys. Chem. C* **123**, 18824 (2019).
- [47] P. Olsson, J. Vidal, and D. Lincot, *J. Phys. Condens. Matter* **23**, 405801 (2011).
- [48] J. Yang, *Thermal Conductivity: Theory, Properties, and Applications* (Kluwer Academic/Plenum Publishers, New York, 2004).
- [49] A. Savin, R. Nesper, S. Wengert, and T. F. Fässler, *Angew. Chemie Int. Ed. English* **36**, 1808 (1997).
- [50] M. K. Jana, K. Pal, A. Warankar, P. Mandal, U. V. Waghmare, and K. Biswas, *J. Am. Chem. Soc.* **139**, 4350 (2017).
- [51] Y. Zhang, E. Skougl, J. Cain, V. Ozoliņš, D. Morelli, and C. Wolverton, *Phys. Rev. B* **85**, 054306 (2012).
- [52] L. Bjerg, B. B. Iversen, and G. K. H. Madsen, *Phys. Rev. B* **89**, 024304 (2014).
- [53] M. D. Nielsen, V. Ozolins, and J. P. Heremans, *Energy Environ. Sci.* **6**, 570 (2013).
- [54] L.-D. Zhao, S.-H. Lo, Y. Zhang, H. Sun, G. Tan, C. Uher, C. Wolverton, V. P. Dravid, and M. G. Kanatzidis, *Nature (London)* **508**, 373 (2014).
- [55] See Supplemental Material at <http://link.aps.org/supplemental/10.1103/PhysRevB.105.245203> for the vibrations of atoms in two transverse acoustic phonon branches (TA and TA'); the partial charge densities at VBM and CBM; the conductivity effective masses (m_e^*), power factors (PF), and figures of merit (ZT) as functions of the carrier concentration for p- and n-type doping at different temperatures in three pyrite-type dichalcogenides, respectively.
- [56] P. B. Allen and J. L. Feldman, *Phys. Rev. B* **48**, 12581 (1993).
- [57] G. A. Akhmedova and D. S. Abidinov, *Inorg. Mater.* **45**, 854 (2009).
- [58] E. S. Toberer, A. Zevkink, and G. J. Snyder, *J. Mater. Chem.* **21**, 15843 (2011).

- [59] O. K. Andersen, *Phys. Rev. B* **12**, 3060 (1975).
- [60] S.-H. Wei and H. Krakauer, *Phys. Rev. Lett.* **55**, 1200 (1985).
- [61] J. Heyd, G. E. Scuseria, and M. Ernzerhof, *J. Chem. Phys.* **118**, 8207 (2003).
- [62] A. V. Krukau, O. A. Vydrov, A. F. Izmaylov, and G. E. Scuseria, *J. Chem. Phys.* **125**, 224106 (2006).
- [63] L. Fu, M. Yin, D. Wu, W. Li, D. Feng, L. Huang, and J. He, *Energy Environ. Sci.* **10**, 2030 (2017).
- [64] Z. M. Gibbs, F. Ricci, G. Li, H. Zhu, K. Persson, G. Ceder, G. Hautier, A. Jain, and G. J. Snyder, *Npj Comput. Mater.* **3**, 8 (2017).
- [65] J. Cao, J. D. Querales-Flores, A. R. Murphy, S. Fahy, and I. Savić, *Phys. Rev. B* **98**, 205202 (2018).